

Solvating magnesium polysulfides enables low-barrier speciation for magnesium sulfur batteries

Received: 6 August 2025

Accepted: 24 February 2026

Published online: 10 March 2026

Check for updates

Jiayi Li¹, Wanyu Zhao¹✉, Keying Guo¹, Shang Shi¹, Yuegang Zhang² & Xiaowei Yang²✉

Magnesium–sulfur batteries offer high theoretical energy density but suffer from low sulfur utilization and rapid capacity fading. This work identifies the strong Mg^{2+} –polysulfide Coulombic interaction as responsible for sluggish kinetics. We demonstrate that the solvation of magnesium polysulfides fundamentally governs their behavior, relaxing Mg^{2+} –polysulfide coupling to facilitate polysulfide speciation and conversion kinetics. Our findings reveal that solvation with high shielding ability effectively modifies the binding configuration of magnesium polysulfides, which lowers the energy barrier for their stepwise conversion, thus improving reaction reversibility. Furthermore, under solvation modulation, magnesium sulfide deposition exhibits a three-dimensional nucleation morphology, providing more active sites for redox. Consequently, the developed cells achieve the equilibrium potential -1.1 V (vs. Mg/Mg^{2+}) and extended cycle life (0.1 C over 120 cycles, 1 C (60 min) = 1675 mA g^{-1}), with pouch cells showing high discharge capacity (940.80 mAh g^{-1} in the 1st cycle; $> 600\text{ mAh g}^{-1}$ after 18 cycles).

Lithium–sulfur batteries (LSBs), known for their high theoretical specific capacity and environmental friendliness, face practical problems such as polysulfide shuttling and lithium dendrite formation^{1–3}. In contrast, magnesium–sulfur batteries (MSBs) have emerged as a prospective alternative, which mitigates the dendrite growth issues and offers a large theoretical volumetric capacity (3833 mAh cm^{-3})^{4–9}. Despite these advantages, the practical development of MSB is hindered by low sulfur conversion efficiency and severe capacity decay^{10,11}. The strong coulombic interactions between Mg^{2+} and polysulfides that significantly retard redox kinetics. Additionally, the poor electronic/ionic conductivity of discharge products, magnesium sulfide (MgS), leads to pore blockage and premature capacity termination¹². To enhance reaction kinetics and optimize battery performance, these critical challenges must be effectively addressed.

The high energy density of MSB originates from multi–electron redox reactions involving complex phase transitions from solid sulfur

to MgS ^{13,14}. During the transition processes, polysulfides (PS) solvated in the electrolyte serve as fundamental intermediates and directly govern the performance of the batteries¹⁵. Prior work has established that strong Mg^{2+} –PS coordination dominates MgPS behavior^{16,17}, but the specific solvation structure of MgPS and its profound influence on the fundamental conversion chemistry itself have remained elusive. Early attempts based on conventional magnesium electrolytes (such as the Grignard reagent/aluminum chloride system) were made, and the instability issue in the presence of polysulfides was pointed out¹⁸. Breakthroughs in the design of electrolyte systems for MSB, such as boron-based and phenolate-based systems with better compatibility, have also been achieved^{19,20}. Besides, recent strategies demonstrate that introducing additives^{21–23} or catalyst²⁴ to the electrolyte can modify the interphase to suppress polysulfide dissolution and diffusion. Nevertheless, the fundamental role of solvent–directed MgPS solvation in steering conversion kinetic and its critical impact on battery performance remain largely unexplored.

¹State Key Laboratory of Synergistic Chem-Bio Synthesis, School of Chemistry and Chemical Engineering, Shanghai Jiao Tong University, Shanghai, China.

²Department of Physics, Tsinghua University, Beijing, China. ✉e-mail: wanyuzhao@sjtu.edu.cn; yangxw@sjtu.edu.cn

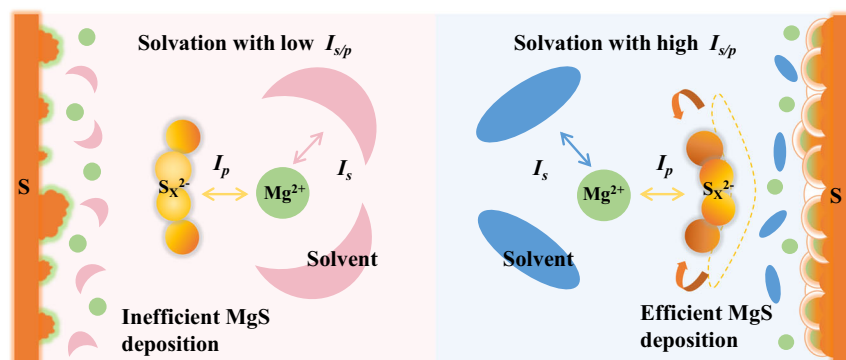


Fig. 1 | Conceptual diagram illustrating the role of solvation modulation in MSB (the pink and blue items represent for the different solvents; the green and orange atoms represent for Mg atoms and sulfur atoms, respectively).

In this work, we reveal that the solvation structure of MgPS is a previously overlooked regulator of the conversion chemistry. To demonstrate this, a series of common ether solvents were selected to evaluate their ability of solvation modulation for MgPSs: 1,2-dimethoxyethane (DME), diethylene glycol dimethyl ether (G2), triethylene glycol dimethyl ether (G3) and tetraethylene glycol dimethyl ether (G4). The lone pair electrons on oxygen atoms of ether solvents enable strong coordination capability, which can stabilize the MgPS complexes. Although these solvents show analogous molecular structures, they demonstrate different electrochemical performance when applied in MSB. To systematically explore the role of solvent, we investigate the solvation-modulated property of polysulfide speciation and explore the relationship between the solvation environment of MgPS and battery performance. We found that solvent shields the interaction between Mg^{2+} and PS and governs MgPS solvation. $I_{s/p}$, calculated by the Mayer bond order ratio of Mg-solvent (I_s) to Mg-PS (I_p), was defined as a parameter to evaluate the shielding ability: solvation environment with high $I_{s/p}$ value exhibits higher shielding ability and exerts stronger effect on the Mg-S interaction, facilitating efficient growth of MgS with the uniform three-dimensional (3D) morphology (Fig. 1). Based on the simulation results, solvents affect the intrachain bonding of polysulfides, which concurrently changes the energy barriers during sulfur conversion. Electrochemical characterization and spectroscopy analysis prove that this solvation effect on MgPS manifest distinctly in voltage profiles, polysulfide conversion, and electrode thermodynamics. Meanwhile, solution-mediated nucleation and growth of MgS also show strong correlation with solvation effect. Among the prepared electrolytes, the G2-based electrolyte, which facilitates a favorable solvation environment with high shielding ability for MgPS, promotes the polysulfide speciation and conversion. High sulfur utilization with 3D morphology deposition of MgS was observed in G2-based electrolyte. Moreover, the G2-based electrolyte demonstrates stable cycling for 120 cycles at 0.1 C in coin cells and exhibits high capacity in pouch cells (940.80 mAh g^{-1} in the 1st cycle; > 600 mAh g^{-1} after 18 cycles), underscoring its suitability for MSBs. These results not only shed light on attainable reaction mechanisms of MgPS speciation and MgS electrodeposition, but also give guidance for solvent selection criteria in designing practical electrolytes for MSB.

Results

Solvation-mediated Mg^{2+} -PS coordination chemistry

Polysulfide species serve as the solvated intermediates in the electrochemical conversion of sulfur electrodes. Their formation and evolution directly govern the energy efficiency, cycling stability, and reaction kinetics of the battery²⁵. To screen the interactions among Mg^{2+} , solvents, and polysulfides and gain deeper insights into the solvation behavior of MgPS, we employed molecular dynamics (MD)

simulations to investigate the structures of polysulfide species in four ether solvents: 1,2-dimethoxyethane (DME), diethylene glycol dimethyl ether (G2), triethylene glycol dimethyl ether (G3) and tetraethylene glycol dimethyl ether (G4). Supplementary Fig. 1 exhibits the radial distribution function (RDF) analyses and coordination numbers in four electrolytes (The atomic coordinates of the optimized structure can be found in the Supplementary Data 1). It can be found that Mg^{2+} not only coordinates with O from the solvents and TFSI⁻ in the solvation shell, but also coordinates with S from polysulfides due to the strong Lewis interaction. Here, the representative reaction intermediate MgS_4 , which bridges the gap in the solid-liquid-solid transformation process, was selected as the focus for a detailed illustration. The solvation structures of MgS_4 derived from electrolytes with different solvents are shown in Fig. 2a. The calculated values of Mayer bond orders and Mulliken charge distribution are listed in Supplementary Tables 1–4. (The solvation structures and corresponding atomic numbers are shown in the Supplementary Fig. 2). According to Supplementary Tables 1–4, it can be seen that for four solvation environments, the terminal sulfur atoms show a more negative Mulliken charge value, indicating a great charge enrichment in two ends of S_4 chain. At the same time, the Mayer order of Mg-S bond exhibits a strong-weak-strong sequence along the S_4 chain and the Mayer bond order of middle S-S bond is weaker than other S-S bonds, suggesting that Mg^{2+} mainly interacts with sulfur atoms at both ends of S_4 . Figure 2b and Supplementary Table 5 demonstrate the average Mayer bond order of Mg-O (I_s) and Mg-S (I_p) in four coordination environments from Fig. 2a. It can be inferred that, due to the strong interaction between Mg^{2+} and PS, I_p is stronger than the I_s for all solvents in Fig. 2b. Moreover, the values of I_s and I_p changes significantly with the solvation environments, indicating solvation shields the strong electrostatic interaction between Mg^{2+} and PS. To assess the role of the solvent on tailoring the solvation structure, the $I_{s/p}$ ratio (the value of I_s divided by the value of I_p) is introduced as a parameter and represents the shielding ability of solvation. Among four solvents, G2-based solvation environment shows the highest $I_{s/p}$ and thus has the strongest effect on MgPSs, indicating effective modulation of Mg-PS interaction. Meanwhile, the Mayer bond order of middle S-S bond in G2-based solvation environment is the weakest (Fig. 2a) and is prone to cleavage, which benefits the MgPS solvation dynamics as well as sulfur conversion kinetics. Moreover, because the high shielding ability of G2, the Mulliken charge of Mg in G2-based solvation environment is the highest (Fig. 2b), suggesting that the valence state of Mg is less influenced. The reaction pathway in the implicit solvation environment by considering the MgS_8 , MgS_4 , and MgS is built in Fig. 2c. Attributed to the solvation effect on the coordination between Mg^{2+} and PS, the energy barrier from solvated polysulfides to terminal solid MgS shows different values. It can be shown that G2 with high shielding ability also facilitates a lower Gibbs free energy change (ΔG), enabling a reduced

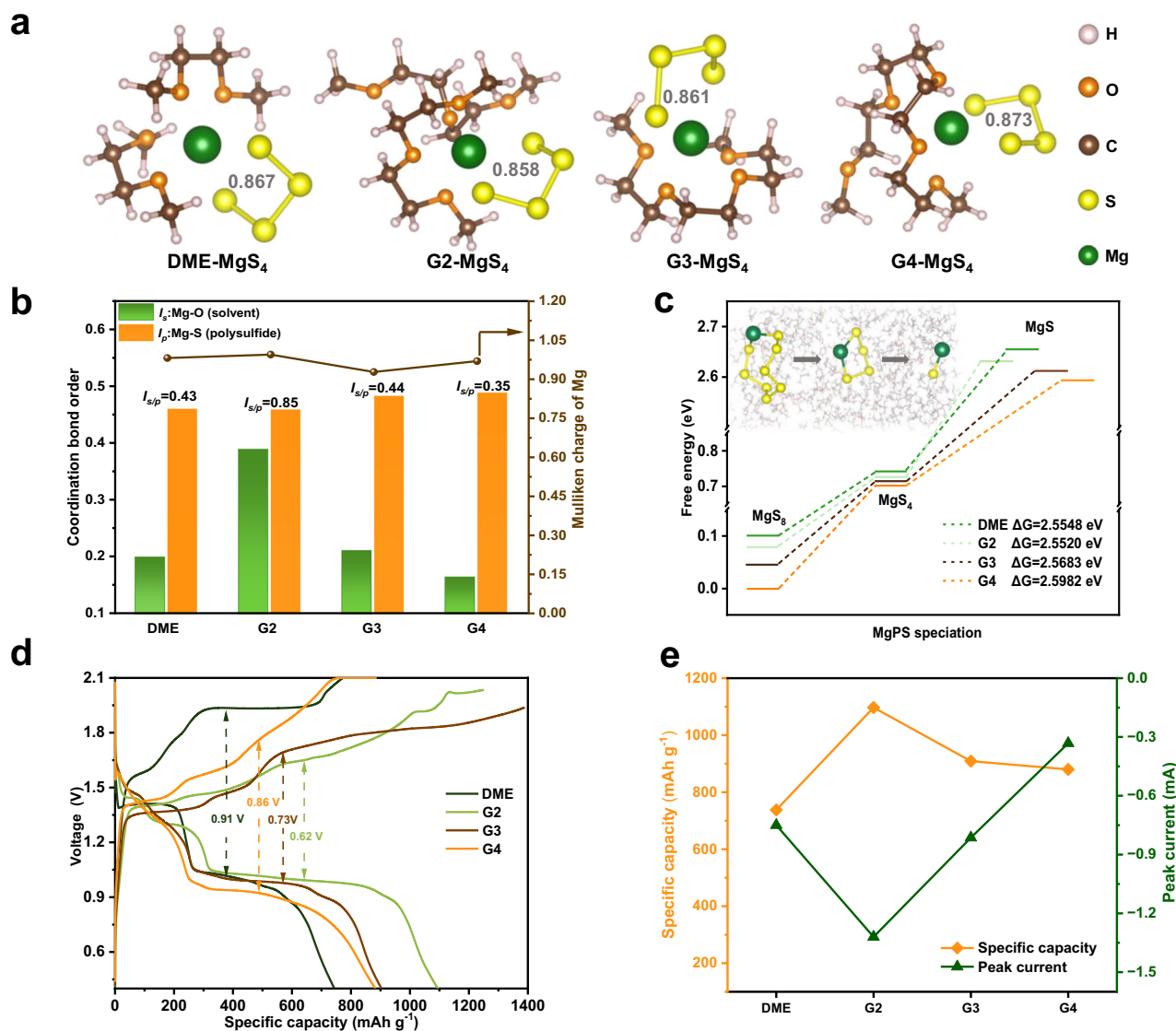


Fig. 2 | Solvation effects on MgPS chemistry and battery performance.

a Comparisons of the solvation shells of MgPS with the middle S-S coordination bond order given by DFT calculations. **b** Coordination bonds of Mg-O (I_s), Mg-S (I_p) and the Mulliken charge of Mg within the solvation structures of MgPS. **c** Gibbs free energy changes of MgS₈, MgS₄ and MgS in four solvent environments (the inset figure shows the conversion of polysulfides within the implicit solvation

environment: the green balls and yellow balls represent the Mg atoms and sulfur atoms, respectively; the stick model in the background represents the solvent environment). **d** Galvanostatic charge-discharge profiles of the electrolytes at 0.05 C in MSB (1 C (60 min) = 1675 mA g⁻¹). **e** Peak current and specific capacities of the batteries.

conversion barrier and accelerated redox kinetics for MgPS. The simulations explicitly decipher the cooperative effects of solvent-Mg²⁺-PS and demonstrate the critical role of solvation mediation in Mg²⁺-PS coordination, providing a molecular-scale basis for MgPS solvation dynamics.

During the charging and discharging process, active sulfur species in both solid and solvated phases control the reaction thermodynamics and provide the capacity²⁶. To figure out how the solvation-mediated intermediates influence the energy density of the battery, constant current charge-discharge and cyclic voltammetry tests were conducted using various electrolyte solvents and iodine additive. The galvanostatic charge-discharge profiles were displayed in Supplementary Fig. 3a-d and the profile of the third cycle at 0.05 C was shown in Fig. 2d. During the discharge reaction, magnesium metal is oxidized, producing Mg²⁺ ions that migrate toward the positive electrode through the separator and electrolyte. Simultaneously, electrons are transferred to the active sulfur materials via an external

circuit to keep the positive electrode at a neutral charge state. It can be concluded that four types of electrolytes exhibited a certain capacity and featured a long plateau with a significant portion of the capacity, originating from the liquid-solid conversion step. Supplementary Fig. 3a shows that in the 1st cycle, DME-based cell shows the high discharge capacity around 1100 mAh g⁻¹ at 0.05 C and exhibits two main voltage plateaus (-1.4 V and -1.0 V). However, because of the irreversible MgS conversion, the high polarization leads to premature termination during charge (coulombic efficiency ~69%), leading to the gradual capacity decay in the following cycles and the cell failure. Based on the discussion in simulation results, it can be inferred that G2 provides the favorable solvation environment for polysulfides, which facilitating the reaction kinetics. Therefore, the charge-discharge profiles of G2-based cell have small polarization (-0.62 V) and reasonably high reversibility during charge and discharge. Meanwhile, the two redox peaks observed at approximately 1.9 V and 2.0 V in Supplementary Fig. 3b attribute to the redox reaction of iodine additive.

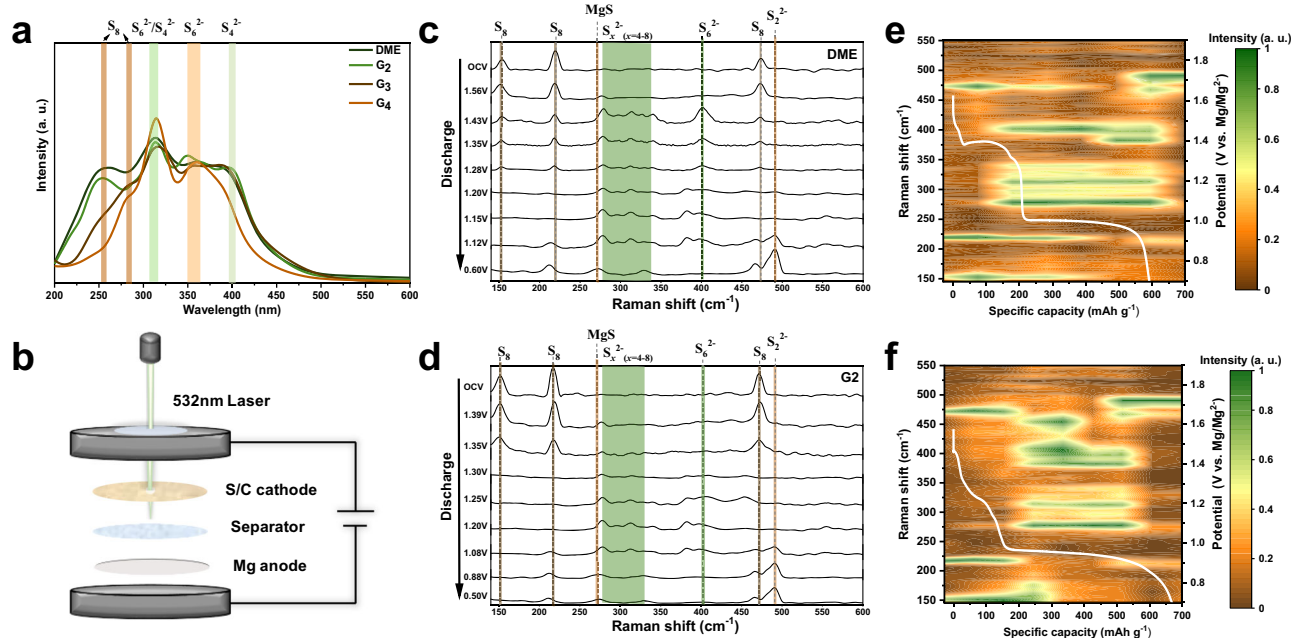


Fig. 3 | Spectroscopic characterization of magnesium polysulfide solvation and conversion. **a** UV-vis absorption spectra of 0.3 mM of MgS_4 in various solvents. **b** Schematic diagram of the operando Raman spectroscopy. Operando Raman

spectra of in MSB with **c** DME and **d** G2 solvent and corresponding contour map **e**, **f** with voltage profile during discharge.

For the G3-based cell, in the first discharge cycle, compared to G2, the solvation environment modulated by G3 has weaker promoting effect on polysulfide conversion, resulting in lower sulfur utilization and reduced capacity release. Notably, unexpectedly prolonged charging profiles near 1.8 V can be observed in the charge curves of G3-based cell in Supplementary Fig. 3c. During this process, the conversion of long-chain polysulfides to short-chain species exhibits slow kinetics, leading to the polysulfide shuttle effect and continuous loss of active sulfur. For G4-based cell, the high viscosity and poor wettability with the electrodes resulted in erratic curve in the first cycle. Then in the following cycles, sulfur undergoes incomplete conversion, which results in low voltage plateaus and low discharge capacity. Furthermore, because of the high dissociation energy barrier of MgS, G4-based cell suffers from a large polarization in charging process, ultimately leading to insufficient charge capacity (Supplementary Fig. 3d). These results confirm that the solvation environment critically determines polysulfide conversion efficiency, with the optimal coordination strength of G2 enabling both low polarization and stable cycling, and this is the core requirements for practical MSBs.

The key results derived from the galvanostatic charge-discharge profiles can be correlated with the CV analysis of four ether-based cells at a scan rate of 0.2 mV s^{-1} (Supplementary Fig. 3e-h). Two main reduction peaks at -1.23 V and -0.88 V were observed both in cells with DME and G2 baseline solvent, which can be attributed to the reaction from long-chain polysulfides to short-chain polysulfides and short-chain polysulfides to MgS, respectively. During charging, the two overlapped oxidation peaks belonged to the MgS oxidation in the G2-based cell start at 1.55 V. In contrast, the cell with the DME solvent shows two separate oxidation peaks at 1.60 V and 1.96 V, which demonstrates a higher energy barrier during the transformation from MgS to elemental sulfur. The small peak at -1.47 V is ascribed to the iodide reduction in the DME- and G2-based electrolyte²⁷. In the case of cells with the G3 and G4 solvent, although the first reduction peak appears around 1.23 V, the peak voltage originated from MgS formation in G3 and G4 is lower than DME and G2, revealing different polysulfides speciation in the electrolyte. Notably, apart from the obvious charge/discharge voltage variations and the pronounced

reduction peak shifts, when comparing the value of peak current and capacities of discharge plateaus (Fig. 2e), it is recognizable that the significant numerical fluctuations exhibit a certain regularity consisted with the replacement of solvent. This variation implies that the electrochemical motive forces for the reversible conversion between elemental sulfur and MgS are drastically changed by solvation of MgPS.

Supplementary Table 6 presents the inherent properties of various solvents, such as viscosity and dielectric constant, which have been proved to have impacts on the sulfur transformation and its reaction mechanism. However, based on the above analysis, these properties cannot independently govern the electrochemical performance. Combined with the molecular simulation, we can comprehensively evaluate the role of solvent and make judgments from a more profound perspective: solvent tunes the coordination of Mg^{2+} -PS and can provide favorable MgPS solvation environment. The feeble binding force of Mg^{2+} toward polysulfide species, coupled with the diminished inter-bond S-S coordination, promotes the acceleration of the reduction reaction via electron acquisition, which contributes to high capacity and reversibility of MSB during the charge/discharge process.

Solvation-mediated MgPS phase transition and nucleation

Redox-active MgPSs play an important role in phase transition at the electrode-electrolyte interface. The solubility of MgPS directly relates to the reaction pathways and kinetic behavior of sulfur, causing following impact on shuttle effect, battery efficiency, and cycling stability for enhancing overall battery performance^{28,29}. Polysulfides dissolved in different solvents with/without iodine additive were analyzed using UV-vis spectroscopy (Fig. 3a and Supplementary Fig. 4). It can be learned that soluble S_8 shows signals at 260 and 280 nm³⁰. Owing to the difference in Donor number (Supplementary Table 6), the intensity of S_8 peak in DME and G2 is higher than G3 and G4. The UV peak at 315 nm attributed to $\text{S}_6^{2-}/\text{S}_4^{2-}$ and the absorbance distributed in 355 and 409 nm belong to S_6^{2-} and S_4^{2-} , respectively³¹. Notably, overlapped with the sulfur peak, the UV peak at 234, 294 and 366 nm originates from iodide ions^{32,33}. The stability of these main intermediates determines the reaction rates of the disproportionation/dissociation/

recombination of polysulfides and thereby affects the phase transition of the MSB.

As illustrated in Fig. 3b, the configuration of Operando Raman spectra was constructed to monitor the MgPS speciation in DME- and G2-based electrolyte during discharge process (Fig. 3c, d). The Raman spectra at open-circuit voltage was obtained, revealing peaks at 155, 218, and 470 cm^{-1} in DME- and G2-based cell, which can be assigned to the signals of elemental sulfur^{34–36}. For DME-based cell, as the voltage decreases, the MgS_x ($x=4-8$) band was observed from 279–325 cm^{-1} , which implies that bulk sulfur is initially reduced, triggering the opening of S8 rings and the formation of liquid-phase chain polysulfides. The band of S_2^{2-} species appears at a high potential of 1.43 V and gradually diminishes with S_x^{2-} ($x=4-8$) as the voltage decreases, while a weak S8 peak can still be detected. In contrast, in the G2 electrolyte, liquid-phase polysulfides emerge at 1.39 V, and their intensity increases gradually during discharge, with almost no detectable S8 peak. This is attributed to the faster conversion of solid-phase S8 to long-chain polysulfides and the subsequent shortening of long-chain polysulfides in the G2 environment, generating the absence of the short plateau region observed around 1.4 V in DME. During the conversion from S to MgS, the step involving the transformation of S_4^{2-} to MgS_2 and MgS contributes to the most capacity³⁷. It can be seen that the band of S_2^{2-} and MgS are observed at 492 and 273 cm^{-1} , respectively. In DME, the S_2^{2-} species appear at a higher potential around 1.12 V and converts rapidly to MgS. However, in the G2 electrolyte, S_2^{2-} species can still be detected at low potentials (0.5 V) and gradually converts to MgS, resulting a longer plateau with more capacity contribution compared to DME. In addition, the solid species S_2^{2-} spans in different voltage range in DME and G2, indicating S nucleation and deposition may relate to solvation.

To further explore the thermodynamic and kinetic properties of MSB during discharge process, galvanostatic intermittent titration technique (GITT) at a current density of 0.05 C was adopted in four ether-based coin cell (Fig. 4a). Each step of GITT was set to be 15 min following 2 h relaxation step in order to ensure the full recovery to thermodynamic equilibrium state (see Supplementary Figs. 5 and 6: Time-dependent potential plots). The corresponding polarizations of the electrochemical reaction in four ether-based cells (Fig. 4b and Supplementary Table 7) were obtained by comparing the equilibrium potential (grey) with the transient potential in Fig. 4a. Obviously, four curves show staging features and the equilibrium potential at long plateau follow a trend of DME (1.125 V) > G2 (1.116 V) > G3 (1.098 V) > G4 (1.088 V). Besides, the polarization status can be divided into three typical stages: S_8 - MgS_x , MgS_x - MgS_2 and MgS_2 - MgS ³⁸. Firstly, active sulfur materials receive electrons through the external electrical circuit, which triggers the successive reduction from elemental sulfur to soluble polysulfides MgS_x (stage 1). Then the soluble polysulfides cleave and convert to solid MgS_2 (stage 2). Solid-state transition from MgS_2 to MgS occurs at the end of the discharge process (stage 3). Stage 1 corresponds to the solid-to-liquid conversion of sulfur to polysulfides in MSB, specifically the dissolution of solid sulfur in the electrolyte environment. A short plateau is observed during this stage, corresponding to the emergence of polysulfides. In the case of G3 and G4, high viscosity leads to wettability issues, which reduces the rate of electrochemical reactions and results in low active material utilization. Consequently, the first plateau exhibits a lower voltage with a distinct sloping profile. In contrast, as seen in the G2 solvent environment, better wettability and higher ionic conductivity allow the active sites on the positive electrode to function effectively and sulfur can readily transform to polysulfides without rapid diffusion away from the reaction interface, thereby resulting in a well-defined plateau region. Meanwhile, DME-based cell suffers from passivation by irreversible residues formed in previous cycles, which hinders the accessibility of active sulfur. This directly leads to the shortage of the plateau and results in incomplete sulfur conversion. In stage 2, long potential

plateau and negligible hysteresis were observed in all curves, indicating that the reaction at this stage is relatively stable and proceeds continuously with lower energy barrier for conversion. Since soluble polysulfides can easily diffuse to the electron available site and acts as redox mediators to transfer electron, the reaction kinetics is faster in stages 1 and 2 than stage 3. For stage 3, the dissolved polysulfides are gradually consumed and high polarization of the solid-state reaction leads to premature termination of the discharge. Moreover, comparing the GITT curves and overpotentials of four ether-based cells, it can be concluded that the stability of the reactions and the ability to overcome the conversion barrier in each stage are relevant to the solvation of the electrolyte. Among the cells, G2-based cell has the smallest variation in polarization and show a more effectively accelerate redox kinetics of the positive electrode. This not only proves the effect of solvation on polysulfides during sulfur reduction, but also illustrates that the charge transfer process and ion diffusion rely on the solvation of the electrolyte³⁹.

Based on the GITT results, it can be found that the unbearable polarization with the sluggish kinetics in stage 3 appears with the MgS nucleation and deposition. During the solid-solid conversion, the morphology and structure of the final product MgS may influence the achievable discharge capacity and the following oxidation process, which directly relates to the utilization and reversibility of active sulfur materials⁴⁰. The quasi-equilibrium potential of MgPS to solid MgS was ascertained by utilizing the potentiostatic intermittent titration technique (PITT). Subsequently, the current-time transients were normalized based on the peak current (i_m) and the corresponding time (t_m ; specific time when the current reaches maximum). Then, the mechanism of MgS electrodeposition was analyzed by fitting the current-time transients to four classical electrodeposition models, including Scharifker-Hills (SH) models⁴¹ (3D instantaneous (3DI) nucleation and 3D progressive nucleation (3DP) nucleation) and Bewick-Fleischman-Thirsk (BFT) models⁴² (2D instantaneous (2DI) nucleation and 2D progressive nucleation (2DP) nucleation). It can be seen that the PITT curves of DME and G2 (Supplementary Fig. 7a and Fig. 4c) show obvious current responses, which is ascribed to the processes of nucleation and growth in liquids/solids. By fitting and analyzing the deposition curves of MgS at the responsive current (corresponding voltage: DME at 0.94 V and 0.80 V; G2 at 0.94 and 0.84 V), the nucleation and growth of MgS in DME- and G2-based electrolytes follow the 3D growth mode, performing a transition from 3DI to 3DP as the discharge proceeds (Supplementary Fig. 8 and Fig. 4d). The 3D precipitation avoids clogging of the positive electrode and exposes more active sites, thereby improving sulfur utilization and stabilizing the electrode structure⁴³. As for G3 and G4, there are no current signals in PITT curves (Supplementary Fig. 7b, c), suggesting that the nucleation mode is not suitable for G3- and G4-based electrolyte.

To further compare the diffusion state of polysulfides in DME and G2, we simulate the polysulfides diffusion and calculate the standard deviation by densities (DME: 0.074; G2: 0.065) (Fig. 5a, b). In DME, the polysulfides exhibit low dispersity and tend to aggregate into clusters on the positive electrode surface, which hinders the conversion and deposition. In contrast, in G2, polysulfides have higher dispersity, enabling better contact with the active sites of the electrode and facilitating more uniform deposition. Nanosized nuclei MgS particles were observed on the carbon paper (CP) via scanning electron microscopy (SEM) (Fig. 5c–f, Supplementary Fig. 9) and confirmed by the EDS (Supplementary Fig. 10). It can be observed that compared with the blank CP, the MgS particles generated in four different solvents all remain spherical shape at a size of 50–100 nm. In DME and G2, the small MgS granules deposit densely on CP and continue to precipitate on top of existing nuclei. Gradually, the particles connect together and the deposition become concentrated, which conforms to 3D nucleation mode. In contrast, in G3 and G4, a small amount of MgS

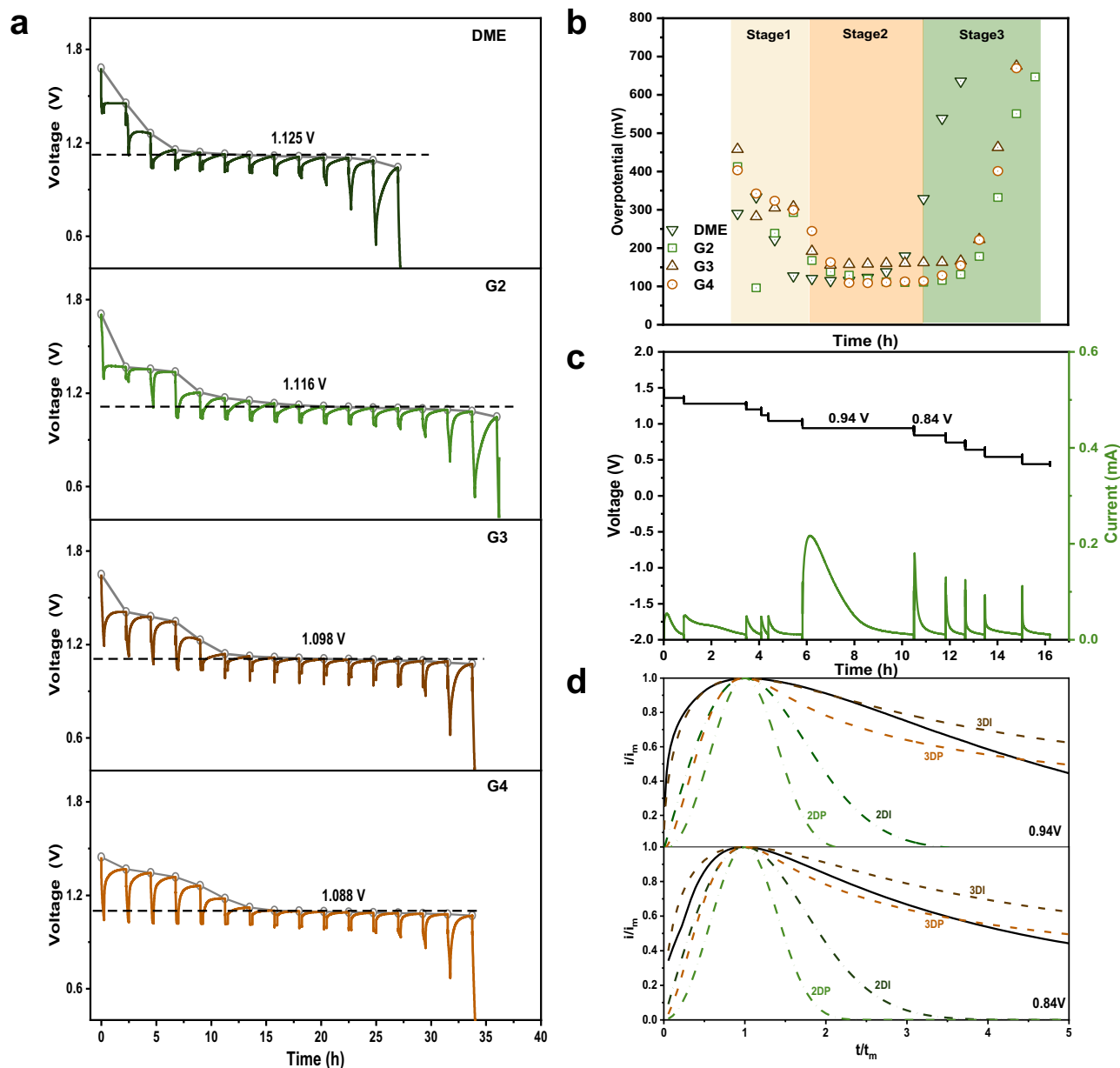


Fig. 4 | Electrochemical kinetic analysis of Mg-S batteries. **a** GITT measurements of MSB in DME and G2 under a repeating constant current pulse of 0.05 C for 15 min followed by a relaxation period of 2 h. **b** Corresponding overpotential of various electrolytes calculated from the GITT results. **c** PITT measurements of MSB in G2

(Current responses until 0.01 mA under -20 mV potential steps). **d** Dimensionless transient (line) in comparison with theoretical 2D and 3D models from PITT measurement of G2 based MSB. i_m : peak current; t_m : time needed to achieve the peak current.

particles are independently deposited on CP. Besides, reducing current density or raising sulfur concentration enhances the compactness of MgS particles (Supplementary Fig. 9b, c). The deposition of MgS on the positive electrode surface after cycling was further confirmed by XPS and TEM characterization (Supplementary Figs. 11 and 12).

Mg-S battery performance evaluation

Based on the preceding discussion and the comprehensive consideration of solvation effect, compared with DME, G3, and G4, the G2-based solvent electrolytes with iodine additive can better enable the operation of MSB. By using the three-electrode cell with Mg metal as the reference electrode, the contribution of G2-based electrolyte to the negative electrode and the positive electrode was clarified (Supplementary Fig. 13). It can be revealed that the three-electrode Mg-S

cell shows similar voltage profile with two-electrode cell (Fig. 2d). The overpotential between Mg stripping and deposition at the negative electrode is only 0.4 V. Meanwhile, the positive electrode exhibits a polarization of -0.7 V between the discharge and charge voltages. What's more, G2-based Mg symmetric cells exhibit cycling performance of over 900 h with low polarization about 0.2 V (Supplementary Fig. 14), identifying the G2-based electrolyte exhibits chemical compatibility with electrophilic sulfur and possesses the capability for reversible magnesium deposition and dissolution. Consequently, G2 solvent is chosen to enhance the performance of MSB. By employing the G2-based electrolyte, the assembled Mg-S full cell exhibits improved performance. CV curves at different scan rates operated in G2-based electrolyte present similar shape and well-maintained redox peaks (A, B, C, D) (Fig. 6a), and there is a linear relationship

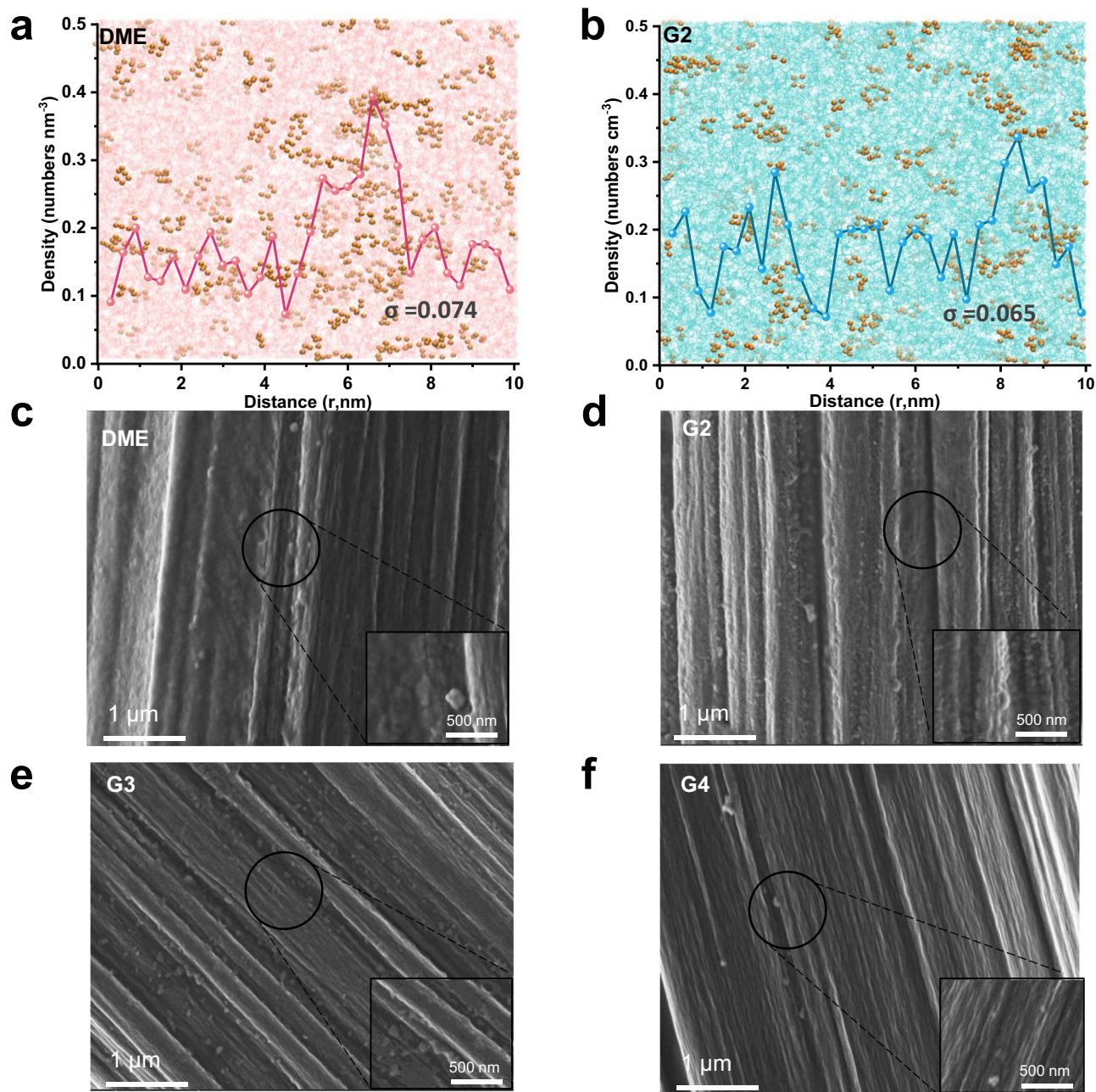


Fig. 5 | Dispersion and morphological characterization of polysulfide behavior. Density profile with snapshots of polysulfides (yellow atoms) in **a** DME (pink) and

b G2 (blue) by MD simulation. σ : the standard deviation of the densities; **c–f** SEM images of MgS deposition on carbon paper in DME, G2, G3, and G4, respectively.

between the peak response currents and square root of scan rates, proving that the highly reversible Mg storage process is driven by diffusion dynamics (Fig. 6b). Rate capability and long-term cycling performance were illustrated in Fig. 6c, d, respectively. It can be found that the G2-based MSB displays a high average specific capacity of 946.61 mAh g⁻¹ at relatively low current density of 0.05 C, which gradually decreases to 350.20 mAh g⁻¹ at 1.0 C, respectively. When the current density was restored to 0.5 C and subsequently to 0.2 C, the MSB presented high restoration capability. Moreover, the G2-based cell demonstrated high cyclic stability over 120 cycles at 0.1 C. The MSB pouch cell with sulfur loading of -1 mg cm⁻² was also assembled and the open-circuit voltage maintained around -2 V (Fig. 6e). The voltage profiles of the pouch cell are displayed in Fig. 6f, showing the performance with high discharge capacity of the 1st cycle

(940.80 mAh g⁻¹) and high retention after 18 cycles. The corresponding specific energy are 31.44 Wh kg⁻¹ in the 3rd cycle and 22.87 Wh kg⁻¹ in the 10th cycle (Supplementary Table 8). These results suggest that G2-based electrolyte effectively facilitate kinetics and optimize the performance, demonstrating the prospects for practical MSB.

According to the above observations and analysis, we demonstrate that strategic solvent selection enables precise control over the solvation structures of MgPS, directly governing polysulfide speciation and ultimately dictating the morphology and reversibility of MgS deposition (Fig. 7). The sulfur reduction pathway initiates with the direct electrochemical conversion of solid S₈ to S₈²⁻ on the electrode-electrolyte interface, followed by its stepwise dissociation into short-chain species. In the solvation environment of MgPS, solvent shields the high electrostatic interaction between PS and Mg²⁺,

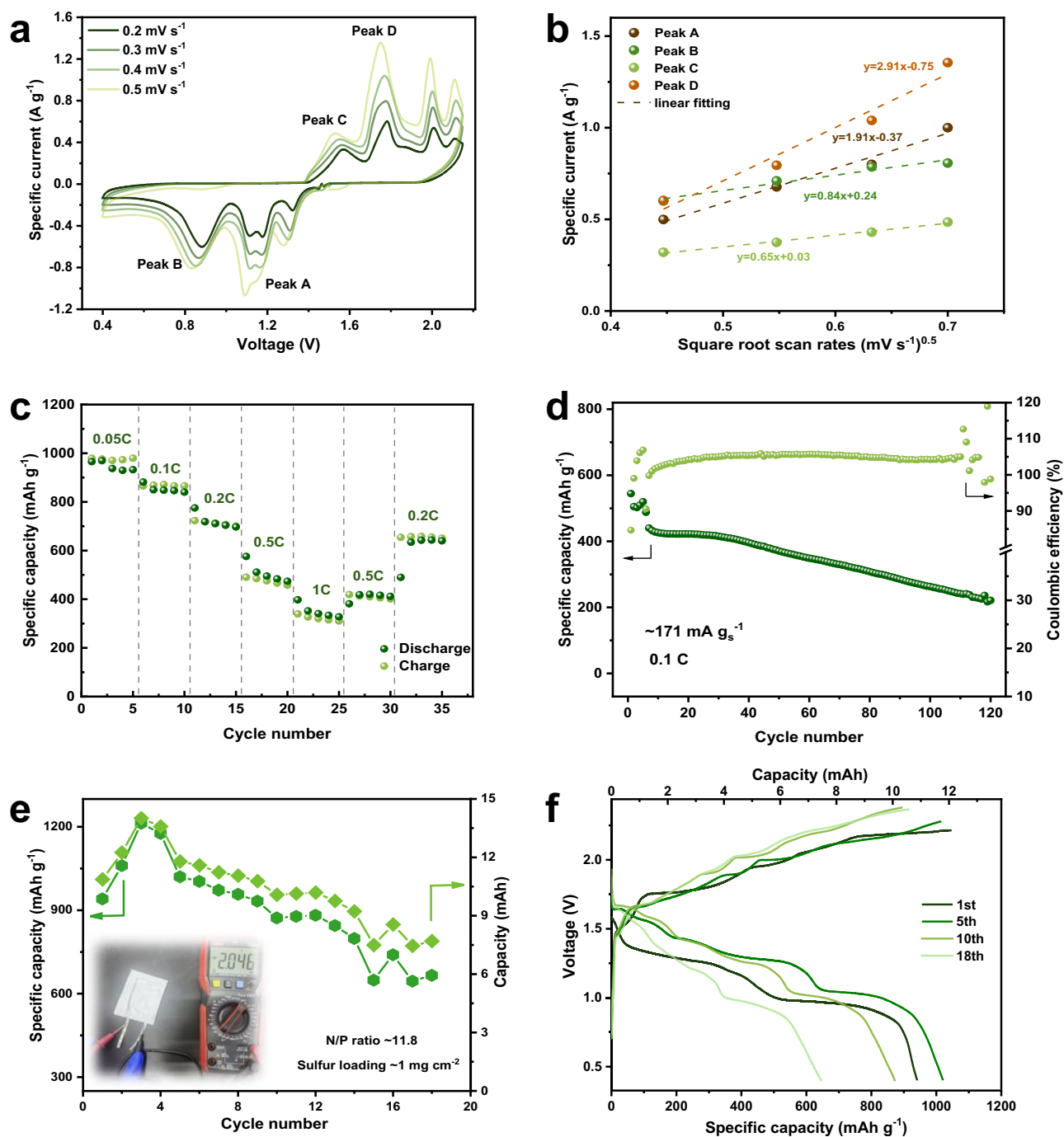


Fig. 6 | Electrochemical properties of G2-based MSB. **a** CV curves at scanning speed from 0.2 mV s^{-1} to 0.5 mV s^{-1} and **b** linear fitting of the peak current (absolute value) versus the square root of the scanning rates. **c** Rate performance from 0.05

to 1C (1C (60 min) = 1675 mA g^{-1}) and **d** cycling performance for 120 cycles at 0.1C. **e** Cycling performance (the inset figure shows the initial open circuit voltage) and **f** voltage–capacity profiles of the pouch cell.

which attenuates the bonding strength of Mg^{2+} –PS and activates the cleavage steps of the polysulfides. Facilitated by the supply of external electrons, MgPS subsequently migrate to the electrode–electrolyte interface and achieve phase conversion. Benefitting from the optimized solvation environment, MgPS contact well with the active sites of the electrode by diffusion force and the formed MgS performs uniform deposition, promoting a 3D morphology nucleation. The 3D nucleation provides efficient charge transfer and improves the utilization rate of sulfur. The continuous growth of MgS is inevitably impeded because of the electron-insulating property, so the consequent deposition mainly depends on the conversion of MgPS.

During this process, under the solvation effect, the MgPS with a strong affinity to the solid particles prefers to deposit on the pre-existing particles along the 3D directions, constructing an ideal interphase and enhancing the reversibility of MgS conversion.

Discussion

MgPS as the precursors of electrochemical deposition are crucial intermediates in sulfur redox reactions, yet the high charge density of Mg^{2+} creates strong interactions with polysulfides, severely limiting their solvation and stabilization. In this study, we draw the correlation between solvent and the regulation of polysulfide speciation and

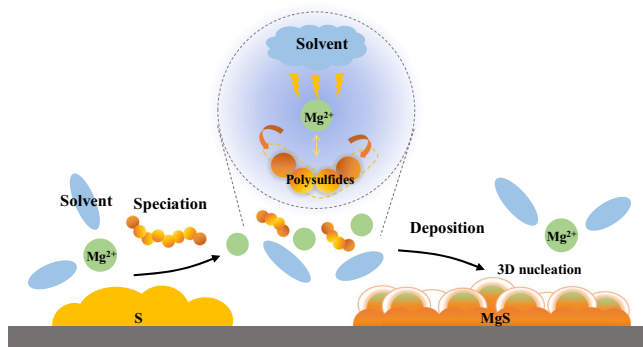


Fig. 7 | The schematic illustration of solvation-modulated phase transition and nucleation.

deposition for kinetic advancement. Specifically, solvent modulates the coordination between Mg^{2+} and PS and solvation with high shielding ability effectively modifies the binding configuration of MgPS , which directly controls the conversion reaction of MgPS . By systematically evaluating four electrolytes, we identified that solvation effect significantly influences voltage profile, MgPS speciation, and thermodynamics process of the sulfur reaction. Spectroscopic analyses including UV–vis absorption spectra and Operando Raman spectra demonstrate that the solvent dictates the speciation and conversion kinetics of polysulfides. Furthermore, solvation-dependent kinetics of sulfur degradation and MgS electrodeposition were also elucidated. Among the prepared electrolytes, the G2-based electrolyte emerges as the most promising. Accordingly, the G2-based full cell enables long cycle life and high capacity. This investigation provides substantial advancements in the fundamental understanding of MSB, promotes an intrinsic understanding of MgPS speciation and MgS nucleation, and offers a solvent selection framework to minimize the gap between theoretical and practical capacities.

Methods

General Materials

$\text{Mg}(\text{TFSI})_2$ (99.5%, Duoduo Chemical Reagent Co., Ltd) was vacuum-dried at 200 °C for 24 h before using. Magnesium sulfide (MgS , 99.98%, Adamas) and iodine (99.995%, Adamas) were sourced from Adamas-beta. Sulfur/carbon composites (S/C, 99.5%) were obtained from Xiamen TOB New Energy Technology Co., Ltd. Polyvinylidene difluoride (PVDF) and Super-P were obtained from Shenzhen Kejing Star Technology Co., Ltd. Solvents including 1,2-dimethoxyethane (DME, 99.5%), diethylene glycol dimethyl ether (G2, 99.5%), triethylene glycol dimethyl ether (G3, 99.5%), tetraethylene glycol dimethyl ether (G4, 99.5%), dimethyl sulfoxide (DMSO, 99.5%) and N-Methylpyrrolidone (NMP, 99.9%) were all purchased from Adamas-beta and dried by molecular sieves (4 Å, Adamas-beta) for over 24 hours before using. All chemicals were used as received.

Synthesis of the electrolyte and magnesium polysulfides (MgPS) solution

The 0.5 M $\text{Mg}(\text{TFSI})_2$ electrolytes were prepared by dissolving dried $\text{Mg}(\text{TFSI})_2$ in DME, G2, G3, and G4, respectively. After 24 h of standing, iodine was added to achieve a final concentration of 0.5 M $\text{Mg}(\text{TFSI})_2$ –0.1 M iodine electrolytes. Then, they were kept at 25 °C for 3 days to ensure the components were well mixed.

Magnesium polysulfide (MgS_x) was synthesized by reacting MgS and elemental sulfur in a 1:3 molar ratio in DMSO under continuous stirring at 70 °C for 6 days to ensure complete dissolution and homogeneous reaction. Subsequently, the solution was vacuum-dried under 70 °C for 48 h to obtain polysulfide powders. The powders were then dissolved in solvents of DME, G2, G3, and G4 with/without iodine

additive to prepare the MgS_x solution. All preparation steps described above were performed in an argon-filled glove box, with both water and oxygen concentrations maintained below 0.1 ppm.

Preparation of S electrodes

The positive electrodes were prepared using the homogeneous slurry mixed from S/C, Super P, and PVDF in a 7:2:1 weight ratio in NMP. The slurry was cast onto Cu foils (16 μm, SHENZHEN KEJING STAR TECHNOLOGY CO., LTD) by doctor blade, followed by vacuum heating of the electrode at 50 °C for 12 h. The dried electrodes were cut into discs with a diameter of 12 mm for cell assembly. The active sulfur loading was around 0.6–1.0 $\text{mg}_{\text{sulfur}} \text{cm}^{-2}$.

Electrochemical measurements

Cell assembly were all carried out in an argon-filled glove box with water and oxygen contents <0.1 ppm. Electrochemical testing was conducted at 25 °C. The ionic conductivity of the electrolytes was measured using a conductivity meter (Mettler Toledo). To make coin cells (CR2025-type) for electrochemical tests, the glass fibre separator (GF/D, thickness of 675 μm, Whatman) was cut into 19-mm-diameter discs and vacuum-dried overnight at 120 °C. A piece of S cathode (diameter of 12 mm) and Mg foil ($1 \times 1 \text{ cm}^2$, Shenzhen Kejing Star Technology Co., Ltd) were separated by the GF/D separator with 90 μl of electrolyte. The galvanostatic charge–discharge tests were conducted at 0.05 C (0.08 A g^{-1}) or 0.1 C (0.17 A g^{-1}) using the NEWARE battery test system. The cut-off potential ranges employed were 0.4–2.2 V for DME, 0.4–2.0 V for G2, 0.4–1.9 V for G3, and 0.4–2.1 V for G4, respectively. Corresponding cyclic voltammetry (CV) measurements were carried out on an IVIUMnSTAT analyzer at a sweep rate of 0.2 mV s^{-1} with the same respective potential ranges. The three-electrode electrochemical tests were conducted in hermetically sealed Teflon Swagelok cell. For the galvanostatic intermittent titration technique (GITT) tests, the cells were activated for 1 cycle and discharged at 0.05 C for 15 min followed by relaxation at open circuit for 2 h in each step. For the PITT test, the cell was potentiostatically discharged with current responses until the current was below 0.01 mA under –20 mV potential steps. The cells for MgS nucleation were assembled using carbon paper (CP, HCP020N) as the working electrode, magnesium foil as the counter electrode and Celgard 2325 as separator. A volume of 20 μL of MgS_x catholyte was applied onto the CP, while 20 μL of the corresponding MgS_x free electrolyte was added to the negative electrode compartment.

The rate performance and cycling performance of the Mg–S coin cells were assembled using positive electrodes with 0.62 $\text{mg}_{\text{sulfur}} \text{cm}^{-2}$ and 0.91 $\text{mg}_{\text{sulfur}} \text{cm}^{-2}$, respectively. The Coulombic efficiency is calculated by the ratio of charge capacity to discharge capacity. The pouch cells (one layer) were fabricated incorporating the negative electrode (Mg foil, $3 \times 4 \text{ cm}^2$, thickness of 50 μm), positive electrode with S loading of -1 mg cm^{-2} ($3 \times 4 \text{ cm}^2$), 200 μL electrolyte and GF/A separator ($3 \times 4 \text{ cm}^2$, thickness of 260 μm, Whatman). Mg foils were freshly polished before being applied. Ni tabs (Shenzhen Kejing Star Technology Co., Ltd) were used for assembly. The cycling was performed at 0.1 C without external pressure applied during cycling. The specific energy of pouch cell is calculated based on the information listed in Supplementary Table 8. The calculation of the specific energy (W) follows:

$$W = \frac{C \times U}{M}$$

Here, C stands for the cell capacity. U represents the average discharge voltage and M represents the total weight. The mass of the packaging and tabs was not taken into the calculations. For each electrochemical condition, a minimum of five cells were evaluated and the performance curves presented in the main figures were derived from a

representative cell that best reflects the median or typical behavior observed across all replicates.

Materials characterization

Ultraviolet–visible (UV–vis) spectra of MgS_x were detected on a Shimadzu UV2600 UV–vis spectrometer. Operando Raman spectroscopy monitor under a 532 nm laser was detected with a perforated stainless steel positive case and a quartz window. The cell was prepared by the stainless steel collector (300 mesh, nominal pore size 40 μm , diameter of 12 mm discs) coated with the positive electrode materials (sulfur loading: 1.0 mg cm^{-2}), Celgard 2325 separator, negative electrode (Mg, diameter of 12 mm discs), and 90 μL electrolyte. Each spectrum was acquired for 20 s with the frequency of 10%. The cells were tested at a current rate of 0.1 C (167.5 mA g^{-1}). The Raman signals were acquired with a Raman microscope (Renishaw, British). XPS analysis was performed after five cycles. All spectra were measured after treating the sample for 10 min by Ar sputtering to remove impurities formed from the XPS instrument chamber as well as the oxide film formed during the sample transport. X-ray photoelectron spectroscopy (XPS) investigations were carried out with ULVAC-PHI, GENESIS 900, and the binding energies were calibrated against the C 1s reference peak. Small electrode fragments were taken out after the potentiostatic discharging tests. The samples were washed with the corresponding solvent to remove additional $\text{Mg}(\text{TFSI})_2$. Samples for transmission electron microscope (TEM, Talos F200X G2), tests were prepared after further sonication of the positive electrode in corresponding solvents and loaded onto a Cu grid. All samples were vacuum dried overnight before transferring to the microscope chamber. The microstructures of MgS on CP were revealed using scanning electron microscopy (SEM, Apreo 2S) accompanied an energy dispersive X-ray spectrometer (EDS).

Theoretical calculation

Density functional theory (DFT) calculations for geometry optimization were conducted by Gaussian 16 software package⁴⁴. Geometry optimizations and energy calculations were performed using B3LYP/6–311 G(d,p)⁴⁵, and the convergence tolerance quality was the default. The solvation effect was considered with the universal solvation model based on density (SMD)^{46,47}.

All the classic molecular dynamic simulations conducted in this work were performed using the Large-scale Atomic/Molecular Massively Parallel Simulator (LAMMPS, <http://lammps.sandia.gov>). OPLS-AA⁴⁸ parameters with 1.14*CMIA partial atomic charges were generated by LigParGen^{49–51} for the organic solvent molecules. The OPLSAA force field developed by Jorgensen was used for Mg^{2+} ⁵². To get the electrolyte structure, isothermal-isobaric (NPT) ensemble runs were first performed at 328 K for 5 ns and then 298 K/328 K for 5 ns to ensure the equilibrium salt dissociation⁵³. Then, 5 ns long canonical (NVT) ensemble runs were conducted and the last 0.5 ns were used to obtain the structure of electrolyte.

Data availability

The original data generated in this study are provided in the Source data file. Source Data file has been deposited in Figshare under accession code DOI link. [<https://doi.org/10.6084/m9.figshare.31047571>]⁵⁴. Extra data are available on request from the corresponding author.

References

- Lin, Y. et al. Organic liquid electrolytes in Li-S batteries: actualities and perspectives. *Energy Storage Mater.* **34**, 128–147 (2021).
- Pang, Q., Liang, X., Kwok, C. Y. & Nazar, L. F. Advances in lithium–sulfur batteries based on multifunctional cathodes and electrolytes. *Nat. Energy* **1**, 16132 (2016).
- Liu, Y. et al. Electrolyte solutions design for lithium-sulfur batteries. *Joule* **5**, 2323–2364 (2021).
- Zhang, Z. et al. Progress and prospects for solving the “shuttle effect” in magnesium-sulfur batteries. *Energy Storage Mater.* **62**, 102933 (2023).
- Kong, L. et al. A review of advanced energy materials for magnesium–sulfur batteries. *Energy Environ. Mater.* **1**, 100–112 (2018).
- Shi, Y. et al. Wetting sub-nanochannels via ionic hydration effect for improving charging dynamics. *Green. Energy Environ.* **9**, 473–480 (2024).
- Fan, Z. et al. Regulating electric double layer via self-assembled monolayer for stable solid/electrolyte interphase on Mg metal anode. *Angew. Chem. Int. Ed.* **64**, e202416582 (2025).
- Zhang, M. et al. Contact ion-pair-dominated electrolyte enabling inorganic-rich solid–electrolyte interphase for long-cycling magnesium metal anodes. *ACS Energy Lett.* **10**, 552–561 (2025).
- Zhao, W. et al. Tailoring coordination in conventional ether-based electrolytes for reversible magnesium-metal anodes. *Angew. Chem. Int. Ed.* **61**, e202205187 (2022).
- Li, Z. et al. Addressing the sluggish kinetics of sulfur redox for high-energy Mg–S batteries. *Adv. Energy Mater.* **13**, 2302905 (2023).
- Chen, S. P. et al. Research status and prospect of separators for magnesium-sulfur batteries. *J. Energy Chem.* **87**, 225–246 (2023).
- Vincent, S., Chang, J. H., Canepa, P. & Garcia-Lastra, J. M. Mechanisms of electronic and ionic transport during Mg intercalation in Mg–S cathode materials and their decomposition products. *Chem. Mater.* **35**, 3503–3512 (2023).
- Lu, Y. et al. Progress and perspective on rechargeable magnesium–sulfur batteries. *Small Methods* **5**, 2001303 (2021).
- Guan, Q. et al. Prospect of cascade catalysis in magnesium-sulfur battery from desolvation to conversion reactions. *Adv. Sci.* **12**, e70008 (2025).
- Luo, T. et al. Polysulfides in magnesium-sulfur batteries. *Adv. Mater.* **36**, e2306239 (2023).
- Bieker, G., Küpers, V., Kolek, M. & Winter, M. Intrinsic differences and realistic perspectives of lithium-sulfur and magnesium-sulfur batteries. *Commun. Mater.* **2**, 37 (2021).
- Zou, Q., Sun, Y., Liang, Z., Wang, W. & Lu, Y. C. Achieving efficient magnesium–sulfur battery chemistry via polysulfide mediation. *Adv. Energy Mater.* **11**, 2101552 (2021).
- Kim, H. S. et al. Structure and compatibility of a magnesium electrolyte with a sulphur cathode. *Nat. Commun.* **2**, 427 (2011).
- Zhang, Z. et al. Novel design concepts of efficient Mg-ion electrolytes toward high-performance magnesium–selenium and magnesium–sulfur batteries. *Adv. Energy Mater.* **7**, 1602055 (2017).
- Li, S. et al. Cation replacement method enables high-performance electrolytes for multivalent metal batteries. *Nat. Energy* **9**, 285–297 (2024).
- Lin, Q. et al. Dual-interface regulation for high-performance magnesium–sulfur batteries. *Adv. Funct. Mater.* **35**, 2506192 (2025).
- Imura, R. et al. Ca^{2+} -driven enhancement of anodic performance and sulfur utilization for magnesium–sulfur batteries. *ChemSusChem* **18**, e202500999 (2025).
- Li, Y. et al. Toward high-performance Mg/S batteries with M4-assisted $\text{Mg}(\text{AlCl}_4)_2/\text{PYR14TFSI}/\text{DME}$ electrolyte and $\text{MoS}_2@\text{CMK}/\text{S}$ cathode. *Small* **20**, e2307396 (2023).
- Xu, Y. et al. Improving a Mg/S battery with YCl_3 additive and magnesium polysulfide. *Adv. Sci.* **6**, 1800981 (2018).
- Li, X.-Y. et al. Polysulfide chemistry in metal-sulfur batteries. *Chem. Soc. Rev.* **54**, 4822–4873 (2025).

26. Liu, J., Zhou, Y., Yan, T. & Gao, X.-P. Perspectives of high-performance Li-S battery electrolytes. *Adv. Funct. Mater.* **34**, 2309625 (2024).
27. Wu, W., Wang, S., Lin, L., Shi, H.-Y. & Sun, X. A dual-mediator for a sulfur cathode approaching theoretical capacity with low overpotential in aqueous Zn-S batteries. *Energy Environ. Sci.* **16**, 4326–4333 (2023).
28. Cañas, N. A., Fronczek, D. N., Wagner, N., Latz, A. & Friedrich, K. A. Experimental and theoretical analysis of products and reaction intermediates of lithium-sulfur batteries. *J. Phys. Chem. C.* **118**, 12106–12114 (2014).
29. He, P. & Schaefer, J. L. The key role of magnesium polysulfides in the development of Mg-S batteries. *ACS Energy Lett.* **7**, 4352–4361 (2022).
30. He, P. et al. Stability and disproportionation of magnesium polysulfides and the effects on the Mg-polysulfide flow battery. *J. Electrochem. Soc.* **168**, 110516 (2021).
31. Häcker, J. et al. Operando UV/vis spectroscopy providing insights into the sulfur and polysulfide dissolution in magnesium-sulfur batteries. *ACS Energy Lett.* **7**, 1–9 (2021).
32. Du, C., Liu, B., Hu, J. & Li, H. Determination of iodine number of activated carbon by the method of ultraviolet-visible spectroscopy. *Mater. Lett.* **285**, 129137 (2021).
33. Kireev, S. V. & Shnyrev, S. L. Study of molecular iodine, iodate ions, iodide ions, and triiodide ions solutions absorption in the UV and visible light spectral bands. *Laser Phys.* **25**, 075602 (2015).
34. Vinayan, B. P. et al. Insights into the electrochemical processes of rechargeable magnesium-sulfur batteries with a new cathode design. *J. Mater. Chem. A* **7**, 25490–25502 (2019).
35. Muthuraj, D. et al. Magnesium polysulfide catholyte (MgS_x): synthesis, electrochemical and computational study for magnesium-sulfur battery application. *J. Power Sources* **486**, 229326 (2021).
36. Tian, J.-H. et al. In situ/operando spectroscopic characterizations guide the compositional and structural design of lithium-sulfur batteries. *Small Methods* **4**, 1900467 (2020).
37. Li, P., Razaq, R. & Bo, S.-H. Intercalation-conversion and displacement-conversion strategies in magnesium-sulfur batteries. *ACS Appl. Energy Mater.* **7**, 11343–11351 (2024).
38. Gao, T. et al. Thermodynamics and kinetics of sulfur cathode during discharge in Mg(TFSI)₂-DME electrolyte. *Adv. Mater.* **30**, 1704313 (2018).
39. Chen, Z.-X. et al. Cathode kinetics evaluation in lean-electrolyte lithium-sulfur batteries. *J. Am. Chem. Soc.* **145**, 16449–16457 (2023).
40. Li, Z., Zhou, Y., Wang, Y. & Lu, Y.-C. Solvent-mediated Li₂S electrodeposition: a critical manipulator in lithium-sulfur batteries. *Adv. Energy Mater.* **9**, 1802207 (2019).
41. Scharifker, B. & Hills, G. Theoretical and experimental studies of multiple nucleation. *Electrochim. Acta* **28**, 879–889 (1983).
42. Bewick, A., Fleischmann, M. & Thirsk, H. R. Kinetics of the electrocrystallization of thin films of calomel. *Trans. Faraday Soc.* **58**, 2200–2216 (1962).
43. Chen, L. et al. Dissociation-precipitation chemistry of lithium polysulfides and its correlation to dynamic evolution of cathode-electrolyte interphase in highly solvating electrolyte. *Angew. Chem. Int. Ed.* **64**, e202423046 (2025).
44. Frisch, M. J. et al. Gaussian 16 Rev. A.03 (Gaussian Inc., 2016).
45. Becke, A. D. Density-functional thermochemistry. III. The role of exact exchange. *J. Chem. Phys.* **98**, 5648–5652 (1993).
46. Marenich, A. V., Cramer, C. J. & Truhlar, D. G. Universal solvation model based on solute electron density and on a continuum model of the solvent defined by the bulk dielectric constant and atomic surface tensions. *J. Phys. Chem. B* **113**, 6378–6396 (2009).
47. Li, R. et al. Data-driven design of advanced magnesium-battery electrolyte via dynamic solvation models. *Energy Environ. Sci.* **18**, 6790–6798 (2025).
48. Jorgensen, W. L., Maxwell, D. S. & Tirado-Rives, J. Development and testing of the OPLS all-atom force field on conformational energetics and properties of organic liquids. *J. Am. Chem. Soc.* **118**, 11225–11236 (1996).
49. Jorgensen, W. L. & Tirado-Rives, J. Potential energy functions for atomic-level simulations of water and organic and biomolecular systems. *Proc. Natl. Acad. Sci. USA* **102**, 6665–6670 (2005).
50. Dodda, L. S., Vilseck, J. Z., Tirado-Rives, J. & Jorgensen, W. L. 1.14*CM1A-LBCC: localized bond-charge corrected CM1A charges for condensed-phase simulations. *J. Phys. Chem. B* **121**, 3864–3870 (2017).
51. Dodda, L. S., Cabeza de Vaca, I., Tirado-Rives, J. & Jorgensen, W. L. LigParGen web server: an automatic OPLS-AA parameter generator for organic ligands. *Nucleic Acids Res.* **45**, W331–w336 (2017).
52. Wang, J., Wang, W., Kollman, P. A. & Case, D. A. Automatic atom type and bond type perception in molecular mechanical calculations. *J. Mol. Graph. Modell.* **25**, 247–260 (2006).
53. Beglov, D. & Roux, B. Finite representation of an infinite bulk system: Solvent boundary potential for computer simulations. *J. Chem. Phys.* **100**, 9050–9063 (1994).
54. Li, J. et al. Solvating magnesium polysulfides enables low-barrier speciation for magnesium sulfur batteries. Figshare, <https://doi.org/10.6084/m9.figshare.31047571> (2026).

Acknowledgements

This work was supported by the National Key Research and Development Program of China (2021YFA1101300, X.Y.), the National Natural Science Foundation of China (Grant Nos. 22225801, W2441009, 22178217, X.Y., 22408228, W.Z.), and State Key Laboratory of Advanced Technology for Materials Synthesis and Processing (Wuhan University of Technology)(W.Z.).

Author contributions

J.L. performed experiments and analyzed the data. J.L. and W.Z. wrote the manuscript. K.G. participated in the discussion of MgPS phase transition and nucleation. S.S. participated in the discussion of data calculation. Y.Z. discussed the results. X.Y. directed this project and supervised the study.

Competing interests

The authors declare no competing interests.

Additional information

Supplementary information The online version contains supplementary material available at <https://doi.org/10.1038/s41467-026-70598-7>.

Correspondence and requests for materials should be addressed to Wanyu Zhao or Xiaowei Yang.

Peer review information *Nature Communications* thanks Ajit Kumar, Guang Yang, and the other anonymous reviewer(s) for their contribution to the peer review of this work. A peer review file is available.

Reprints and permissions information is available at <http://www.nature.com/reprints>

Publisher's note Springer Nature remains neutral with regard to jurisdictional claims in published maps and institutional affiliations.

Open Access This article is licensed under a Creative Commons Attribution-NonCommercial-NoDerivatives 4.0 International License, which permits any non-commercial use, sharing, distribution and reproduction in any medium or format, as long as you give appropriate credit to the original author(s) and the source, provide a link to the Creative Commons licence, and indicate if you modified the licensed material. You do not have permission under this licence to share adapted material derived from this article or parts of it. The images or other third party material in this article are included in the article's Creative Commons licence, unless indicated otherwise in a credit line to the material. If material is not included in the article's Creative Commons licence and your intended use is not permitted by statutory regulation or exceeds the permitted use, you will need to obtain permission directly from the copyright holder. To view a copy of this licence, visit <http://creativecommons.org/licenses/by-nc-nd/4.0/>.

© The Author(s) 2026